Scaling Analysis of Two-Phase Flow in Fractal Permeability Fields

Yuhang Wang[1], Jesse Mckinzie[3], Frederico Furtado[2], Saman A. Aryana[2,3]

[1]Department of Petroleum Engineering, University of Wyoming, Laramie, WY, 82071
[2]Department of Mathematics and Statistics, University of Wyoming, Laramie, WY, 82071
[3]Department of Chemical Engineering, University of Wyoming, Laramie, WY, 82071

Key Points:

- A generalized analytical scaling relation is derived for two-phase flow in permeable media subject to self-similar heterogeneity.
- Numerical results from a high-resolution simulator agree with predictions of the derived scaling relation.
- Nonlinear flows scale with the degree of nonlinearity in the asymptotic regime.

Corresponding author: Saman A. Aryana, saryana@uwyo.edu

Abstract

Fluid mixing in permeable media is essential in many practical applications. The mixing process is a consequence of velocity fluctuations owing to geological heterogeneities and mobility contrast of fluids. Heterogeneities in natural rocks are often spatially correlated, and their properties, such as permeability, may be described using fractal distributions. This work models the fractal characteristics of such permeability fields in which the covariance function is expressed as a power-law function. A generalized scaling relation is derived relating various fractal permeability fields using the magnitude of their fluctuations. This relation reveals the self-similar behavior of two-phase flow in such permeable media. To that end, a recently developed, high-resolution numerical simulator is employed to validate the analytically derived scaling relations. Two flow problems are considered in which flow is governed by 1) a linear, and 2) a nonlinear transport equation. Due to the probabilistic representation of the fractal permeability fields, a sensitivity study is conducted for each flow scenario to determine the number of realizations required for statistical convergence. Scaling analysis is performed using ensemble averages of simulated saturation profiles and their mixing lengths. Results support the validity of the developed scaling relation across the range of investigated flow conditions at intermediate times. The dynamics of linear flow in the asymptotic regime is affected by the correlation structure of heterogeneity. In nonlinear flow, scaling behavior appears to be dominated by the degree of nonlinearity.

Plain Language Summary

Multiphase flow in subsurface permeable media plays a fundamental role in many natural and engineering processes, such as remediation of contaminated aquifers, geological carbon storage, and petroleum reservoir engineering. In all these instances, variability of the media's properties and contrasts of density and viscosity of the flowing phases may lead to significant velocity fluctuation at the pore-scale and mixing of the fluids at the macroscale. Optimal design and exploitation of these subsurface resources require accurate and predictive macroscale descriptions of the flow processes. This work investigates the impact of spatial heterogeneity on flow characteristics using a probabilistic description for the permeability field. We demonstrate a relation between flow behaviors in various self-similar fields with a power-law covariance structure. Our findings may help to predict flow behavior in geological formations without the need to conduct full-scale simulations.

1 Introduction

Flow and transport in permeable media in the context of the subsurface is receiving a growing interest due to the wide range of applications that rely on an in-depth understanding of such processes. Natural permeable media consist of matrices of grains interspersed with interconnected pores. To capture the dynamics of subsurface flow, mathematical modeling and numerical simulation play essential roles. Given the availability of information regarding the exact geometry, pore-scale modeling and simulation studies provide a detailed understanding of interactions between fluids and solids in permeable media (Celia et al., 1995; Prodanović & Bryant, 2006; Bijeljic & Blunt, 2006; Liu et al., 2014; Mehmani & Tchelepi, 2019). An accurate understanding of physical mechanisms of flow and transport at pore-scale is critical to deriving predictive macroscopic descriptions, which account for disparate length scales and are indispensable in simulating flow in large-scale systems. These mathematical descriptions rely on macroscale variables such as saturation, porosity, and permeability, and they are formulated using conservation laws (LeVeque, 1992). Darcy's law is a macroscale expression of the conservation of momentum for single phase flow at low Reynolds numbers (Hubbert, 1957; Whitaker, 1986; Dullien, 2012). In the case of multiphase flow, Darcy's law is extended by incorporating constitutive relations, i.e., relative permeability and capillary pressure functions (Muskat & Meres, 1936; Wyckoff & Botset, 1936; Leverett, 1941). This work investigates two-phase flow in fully saturated permeable media with significant viscous forces, such that Darcy-scale continuum models apply (Wilkinson & Willemsen, 1983; Lenormand, 1990; C. Zhang et al., 2011; F. Guo & Aryana, 2019).

Macroscopic dispersive mixing induced by fluctuations in the velocity field is of considerable interest in a number of practical applications involving multiphase flow in permeable media. Examples include remediation of contaminated aquifers, geological carbon storage, and petroleum reservoir engineering (Mercer & Cohen, 1990; Helmig, 1997; Juanes, 2008; B. Guo et al., 2014; Liang et al., 2018; Yuan et al., 2019). In such flows, the growth of the region where the mixing of fluids occurs is driven by spatial heterogeneity in natural geological media, and nonlinearity inherent in the governing equation due to contrast of fluid properties (Hassan et al., 1997; D. Zhang & Tchelepi, 1999; Furtado & Pereira, 2003; Chen & Durlofsky, 2006; Hajibeygi et al., 2012; Heidari & Li, 2014; Christou et al., 2019). This work focuses on the self-similar behavior in mixing due to heterogeneity associated with permeability fields. Permeability distributions in natural permeable media are often observed to be correlated in space, i.e., they exhibit fractal characteristics. Due to difficul-

ties in complete characterization of their spatial variations, their descriptions often rely on sparse data collected over relatively long distances. A representative description of variations across the field may be incorporated in a stochastic manner on the basis of random fields (Hewett & Behrens, 1990; Neuman, 1995; Eggleston & Rojstaczer, 1998; Babadagli, 2006; Cushman, 2013; Xue et al., 2019), and the heterogeneity may be quantified through fractal dimension or Hurst exponent (Mandelbrot, 1985; Voss, 1988). As suggested in previous studies (Furtado & Pereira, 1998; Borges et al., 2009; Francisco et al., 2014; Daripa & Dutta, 2017), this work adopts the fractal field with a power-law covariance function to characterize permeability fields.

The randomness of the permeability field gives rise to fluctuations in fluid velocities. These fluctuations lead to a mixing region between fluids in the vicinity of the displacement front. The mixing may be characterized by the degree of mixing, which is defined based on the variance of concentration field (Dentz et al., 2011; Jha et al., 2011). Such a method can be applied to quantify the mixing regardless of flow configurations. Previous studies of fluid mixing focus on modeling rectilinear flow through a horizontal cross-section of the permeable media with a line source injection. Under such conditions, the mixing region can be characterized by its extent along the main directions of flow, referred to as the mixing length. The rate of growth of this mixing length has important implications in practical applications. As a result, a major question concerns the growth of the mixing region. Glimm and Sharp (1991) analyzed the relation between the growth of mixing length and the heterogeneity of random (permeability) fields in the case of tracer flow, which is governed by a linear transport equation. The fractal permeability field has a covariance function expressed in the form of a power law with a single exponent. Q. Zhang (1992) generalized the results of Glimm and Sharp (1991) by extending this analysis to a multifractal system, where the permeability field is characterized with scale-dependent exponents (Harte, 2001). Furtado and Pereira (1998) studied fluid mixing for immiscible two-phase flow in heterogeneous permeable media using numerical simulations. Results of tracer flows agree well with theoretical predictions (Glimm & Sharp, 1991). Moreover, in the case of nonlinear flow, results indicate that the underlying heterogeneities play a major role in determining transient behavior of the mixing process, and large-time behavior is independent of the strength and correlation structure of heterogeneities. Borges et al. (2009) derived a scaling relation for tracer flow, which is valid for any strength of the underlying self-similar field. Results from Monte Carlo studies show that the mixing lengths from heterogeneous

fields with different strengths collapse to a single curve once they are scaled according to the developed theory. This finding is similar to the results of scaling analysis for miscible displacements reported by Sajjadi and Azaiez (2013). Despite recent advances in understanding the impact of heterogeneity on fluid mixing for miscible or partially miscible flows (Nicolaides et al., 2015; Connolly & Johns, 2016; Amooie et al., 2017; Nijjer et al., 2019), few studies have explored self-similarity of the evolution of mixing for both miscible and immiscible flows in fractal permeability fields.

In this paper, we revisit two-phase flows in heterogeneous permeable media and we focus on flow regimes where viscous forces dominate and overwhelm capillary forces. As a result, the velocity field plays an essential role in driving the mixing process of two-phase flows. A high-resolution numerical scheme is used to solve the governing equations to reduce numerical diffusion and obtain accurate velocity fields. The classical formulation of the governing equations is expressed as two partial differential equations (PDE): an elliptic PDE for flow quantities, i.e., velocity and pressure, and a hyperbolic PDE for saturation. Finite difference (FD) methods are often used to discretize the elliptic PDE. Implementation of FD schemes suffers from two major drawbacks. First, an accurate solution of the elliptic PDE may require a fine grid size, which results in a large number of grid cells and high computational cost. Second, the inclusion of constitutive relations gives rise to a system of nonlinear PDEs that requires an implicit iterative scheme to eliminate numerical instability. Spectral methods serve as effective alternatives (D. Gottlieb & Orszag, 1977). In such schemes, solution is written as a sum of certain basis functions, e.g., Fourier series. As a consequence, spatial derivatives of primary variables are computed with high-order of accuracy using a Fast Fourier Transform (FFT). Such a method involves $\mathcal{O}\left(N \log N\right)$ operations for N modes, which is much faster than FD schemes whose number of operations is usually given by $(\mathcal{O}\left(N^2\right))$ (Kutz, 2013). Due to their efficiency and accuracy, spectral methods are commonly used in problems involving miscible/immiscible displacements (Tan & Homsy, 1988; Rogerson & Meiburg, 1993; Riaz & Tchelepi, 2006; Yuan & Azaiez, 2014; Wang et al., 2018; Wen et al., 2018; Wang et al., 2019).

In the remainder of this paper, we present the governing equations for two-phase flow, and the computational setup including boundary and initial conditions. We construct scalar permeability fields based on self-similar random fields with a power-law covariance structure. We derive scaling relations for two-phase flow subject to fractal permeability fields analytically. We utilize a spectral method to solve the vorticity stream-function equation,

and a high-order, total variation diminishing (TVD) scheme (Harten, 1983; Sweby, 1984) for spatial discretization of convection flux in the transport equation. Linear transport, e.g., tracer flow, is simulated in heterogeneous permeable media. A statistical convergence study is performed to determine the required number of realizations of the permeability field. Scaling analysis is conducted by applying theoretically derived relations to the results of the numerical simulations in which two values of the scaling exponent are investigated. We then investigate nonlinear transport where the constitutive relation, i.e., relative permeability, is extracted from the literature (Tang & Kovscek, 2011). Two cases are considered regarding the onset of flow instabilities using total shock mobility ratio as its indicator (Berg & Ott, 2012). We perform scaling analysis guided by the derived relations using mean saturation profiles and the length of the associated mixing zones. We close with a discussion of results and conclusion.

2 Mathematical Model

The Darcy-scale formulation for multiphase flow in permeable media is simplified by assuming incompressible and isothermal conditions with constant porosity ϕ. The governing equations are given by

$$\phi \partial_t S_\alpha + \nabla \cdot \boldsymbol{u}_\alpha = q_\alpha, \tag{1}$$

$$\boldsymbol{u}_\alpha = -\frac{k k_{r\alpha}(S_\alpha)}{\mu_\alpha} \nabla P_\alpha, \tag{2}$$

where the subscript α denotes the invading ($\alpha = i$) or the resident phase ($\alpha = r$). S_α, $\boldsymbol{u}_\alpha$, q_α, $k_{r\alpha}$, μ_α, and P_α denote saturation, Darcy velocity, volumetric flow rate, relative permeability, viscosity, and pressure of phase α. We consider equations (1) and (2) in a two-dimensional square domain $\Omega = [0, L] \times [0, L]$ with boundary conditions given by

$$\begin{aligned} \boldsymbol{u} \cdot \boldsymbol{n} &= -U, \text{ on } x = 0, \\ P_i &= 0, \text{ on } x = L, \\ \boldsymbol{u} \cdot \boldsymbol{n} &= 0, \text{ on } y = 0, L, \end{aligned} \tag{3}$$

where $\boldsymbol{n}$ is the unit outward normal vector to $\partial\Omega$. The boundary conditions given by (3) simulate a flow predominantly parallel to the x-axis. The invading phase is injected uniformly at the left boundary ($x = 0$) with constant velocity U, displacing the resident phase initially saturated in Ω. The invading phase pressure is assumed to be constant at the outlet ($x = L$). No-flow boundary conditions are imposed along the horizontal boundaries

($y = 0$ and $y = L$). The Riemann initial condition is expressed as

$$S_i = \begin{cases} S_{im}, & \text{if } x < 0, \\ S_{ir}, & \text{otherwise}, \end{cases} \tag{4}$$

where S_{im} and S_{ir} are maximum and irreducible saturation values of the invading phase, respectively.

A spectral numerical method is used to obtain highly accurate velocity fields: flow equations are written in a vorticity stream-function form (Tryggvason & Aref, 1983; Meiburg & Homsy, 1988; Tan & Homsy, 1988; Rogerson & Meiburg, 1993). The following model is used in subsequent numerical experiments:

$$\begin{cases} \nabla^2 \tilde{\psi} = k\lambda_T(S_i) \left(\nabla \left(\dfrac{1}{k\lambda_T(S_i)} \right) \times \boldsymbol{u} \right) \cdot \hat{\boldsymbol{k}}, \\ \boldsymbol{u} = (u_x, u_y) = (\partial_y \tilde{\psi} + u_x^0, -\partial_x \tilde{\psi}), \\ \phi \partial_t S_i + \nabla \cdot (\boldsymbol{u} f_i(S_i)) = q_i. \end{cases} \tag{5}$$

Here $\tilde{\psi}$ is the fluctuating component of the stream function, ψ, $\hat{\boldsymbol{k}}$ is the unit vector in the positive z-direction, u_x and u_y are scalar components of the total velocity $\boldsymbol{u}$ along x- and y-axes, respectively. $\lambda_T(S_i)$ is the total mobility given by $\lambda_T(S_i) = \lambda_i(S_i) + \lambda_r(S_i)$, and $f_i(S_i)$ is the fractional flow function for the invading phase given by $f_i(S_i) = \lambda_i(S_i)/\lambda_T(S_i)$. Readers are referred to Wang et al. (2018) for the detailed derivation of system (5).

We consider scalar, log-normal permeability fields expressed as

$$k_\rho(\boldsymbol{x}) = k_0 e^{\rho \xi(\boldsymbol{x})}, \tag{6}$$

where k_0 is a constant permeability value, ρ ($\rho > 0$) is a coefficient that sets the strength of fluctuations, and $\xi(\boldsymbol{x})$ is a Gaussian isotropic scalar field characterized by the mean,

$$\langle \xi(\boldsymbol{x}) \rangle = 0, \tag{7}$$

and its two-point covariance function is given by (Glimm & Sharp, 1991)

$$C(\boldsymbol{x}, \boldsymbol{y}) = \langle \xi(\boldsymbol{x}) \xi(\boldsymbol{y}) \rangle = |\boldsymbol{x} - \boldsymbol{y}|^\beta, \tag{8}$$

where angle brackets denote ensemble averaging. β ($\beta < 0$) is the scaling exponent which controls the correlation structure of heterogeneity: a large $|\beta|$ indicates that the covariance function decays quickly, which results in fields with short length scale correlations; on the other hand, as $|\beta|$ decreases, the covariance function decays slower. This produces a smoother field.

3 Scaling Analysis

Here we develop scaling relations which relate flow behavior to the magnitude of heterogeneities. Consider a random field which is related to $\xi(\boldsymbol{x})$ given by

$$\zeta(\boldsymbol{x}) = \gamma(\lambda)\,\xi(\lambda\boldsymbol{x}), \tag{9}$$

where $\gamma(\lambda)$ is dependenet on λ ($\lambda > 0$). The two-point covariance function of $\zeta(\boldsymbol{x})$ is expressed as

$$\langle \zeta(\boldsymbol{x})\,\zeta(\boldsymbol{y})\rangle = \gamma^2 \langle \xi(\lambda\boldsymbol{x})\,\xi(\lambda\boldsymbol{y})\rangle, \tag{10}$$

where

$$\langle \xi(\lambda\boldsymbol{x})\,\xi(\lambda\boldsymbol{y})\rangle = \lambda^{\beta}\,|\boldsymbol{x}-\boldsymbol{y}|^{\beta} \tag{11}$$

based on equation (8). Combining equations (10) and (11), we arrive at

$$\langle \zeta(\boldsymbol{x})\,\zeta(\boldsymbol{y})\rangle = \gamma^2\lambda^{\beta}\,|\boldsymbol{x}-\boldsymbol{y}|^{\beta}\,. \tag{12}$$

$\gamma(\lambda)$ is determined such that fields $\zeta(\boldsymbol{x})$ and $\xi(\boldsymbol{x})$ have identical covariance function, i.e., $\langle \zeta(\boldsymbol{x})\,\zeta(\boldsymbol{y})\rangle = \langle \xi(\boldsymbol{x})\,\xi(\boldsymbol{y})\rangle$. $\gamma(\lambda)$ is given by

$$\gamma(\lambda) = \lambda^{-\beta/2}, \tag{13}$$

and the following relation is obtained:

$$\lambda^{-\beta/2}\xi(\lambda\boldsymbol{x}) = \xi(\boldsymbol{x})\,. \tag{14}$$

Therefore, the permeability field described by (6) satisfies the scaling relation given by

$$k_{\rho_1}(\boldsymbol{x}) = k_{\rho_2}\left(\frac{\sigma_2}{\sigma_1}\boldsymbol{x}\right), \tag{15}$$

where $\sigma_j = \rho_j^{-2/\beta}$. The scaling property given by equation (15) relates solutions to flow problems with random permeability fields k_{ρ_1} and k_{ρ_2}. Indeed, let $\tilde{\psi}_\rho$, $\boldsymbol{u}_\rho$, and S_ρ solve equations (5) with random permeability k_ρ. The Riemann initial condition (4) and the boundary conditions (3) are invariant under the spatial scaling (15). Then, if $\sigma_j = \rho_j^{-2/\beta}$ (as above),

$$\tilde{\psi}_{\rho_1}(\boldsymbol{x},t) = \frac{\sigma_1}{\sigma_2}\tilde{\psi}_{\rho_2}\left(\frac{\sigma_2}{\sigma_1}\boldsymbol{x}, \frac{\sigma_2}{\sigma_1}t\right), \tag{16}$$

$$\boldsymbol{u}_{\rho_1}(\boldsymbol{x},t) = \boldsymbol{u}_{\rho_2}\left(\frac{\sigma_2}{\sigma_1}\boldsymbol{x}, \frac{\sigma_2}{\sigma_1}t\right), \tag{17}$$

and

$$S_{\rho_1}(\boldsymbol{x},t) = S_{\rho_2}\left(\frac{\sigma_2}{\sigma_1}\boldsymbol{x}, \frac{\sigma_2}{\sigma_1}t\right). \tag{18}$$

In particular, if $\bar{S}_\rho(\boldsymbol{x},t) = \langle S_\rho(\boldsymbol{x},t)\rangle$, which denotes the one-dimensional mean saturation profile (averaged in the transverse direction to mean flow), it follows that

$$\bar{S}_{\rho_1}(x,t) = \bar{S}_{\rho_2}\left(\frac{\sigma_2}{\sigma_1}x, \frac{\sigma_2}{\sigma_1}t\right). \tag{19}$$

A quantitative analysis of the mixing process is afforded via the analysis of the growth rate of the mixing region as a function of time. For this purpose, we introduce a time dependent length scale, referred to as the mixing length, given as

$$l(t) \coloneqq \frac{1}{S_- - S_+}\int_0^L \left|\bar{S}(x,t) - S_H(x,t)\right| dx, \tag{20}$$

where S_- and S_+ are saturation values behind and ahead the saturation front from the analytical solution (denoted by S_H) of the Buckley-Leverett equation (Buckley & Leverett, 1942) in a homogeneous system. The scaling relation (19) implies that

$$l_{\rho_1}(t) = \frac{\sigma_1}{\sigma_2} l_{\rho_2}\left(\frac{\sigma_2}{\sigma_1}t\right). \tag{21}$$

4 Numerical Scheme

The velocity field, $\boldsymbol{u}$, is expressed as a function of first-order spatial derivatives of the fluctuating component of the stream function, i.e., $\partial_x\tilde{\psi}$ and $\partial_y\tilde{\psi}$, as shown in (5). To calculate the velocity components, u_x and u_y, the Fourier transform is applied to the first equation in system (5):

$$\mathcal{F}\left(\tilde{\psi}\right) = -\frac{\mathcal{F}\left(k\lambda_T(S_i)\left(\nabla\left(\frac{1}{k\lambda_T(S_i)}\right)\times\boldsymbol{u}\right)\cdot\hat{\boldsymbol{k}}\right)}{\left(k_x^2+k_y^2\right)}, \tag{22}$$

where $\mathcal{F}(\cdot)$ denotes the Fourier transform operator, and k_x and k_y are wave numbers along the x- and y-axes, respectively. $\partial_x\tilde{\psi}$ and $\partial_y\tilde{\psi}$ on the transformed Fourier space are given by (Kutz, 2013)

$$\mathcal{F}\left(\partial_x\tilde{\psi}\right) = ik_x\mathcal{F}\left(\tilde{\psi}\right) \text{ and } \mathcal{F}\left(\partial_y\tilde{\psi}\right) = ik_y\mathcal{F}\left(\tilde{\psi}\right), \tag{23}$$

where i is unit imaginary number. $\partial_x\tilde{\psi}$ and $\partial_y\tilde{\psi}$ are then obtained by performing an inverse transform on both sides of equation (23), resulting in

$$\partial_x\tilde{\psi} = \mathcal{F}^{-1}\left(ik_x\mathcal{F}\left(\tilde{\psi}\right)\right) \text{ and } \partial_y\tilde{\psi} = \mathcal{F}^{-1}\left(ik_y\mathcal{F}\left(\tilde{\psi}\right)\right), \tag{24}$$

where $\mathcal{F}^{-1}(\cdot)$ denotes the inverse Fourier transform operator.

The transport equation in system (5) may be rewritten as

$$\frac{\mathrm{d}S_i}{\mathrm{d}t} \approx L(S_i, \boldsymbol{u}), \tag{25}$$

where $L(\xi, \boldsymbol{u}) = \dfrac{1}{\phi \Delta x \Delta y} C(S_i, \boldsymbol{u})$, $C(S_i, \boldsymbol{u})$ is an approximation to the convection flux. To reduce numerical diffusion arising from the discretization, this work implements the central-upwind scheme (Kurganov & Tadmor, 2000; Kurganov et al., 2001) where the intermediate values are constructed using the third-order weighted essentially nonoscillatory (WENO) scheme (Kurganov & Levy, 2000; Kurganov & Petrova, 2001; Shu, 2009). For details of the discretization of the convection flux, readers are referred to Appendix A. A third-order TVD Runge-Kutta method (S. Gottlieb & Shu, 1998; S. Gottlieb et al., 2001) is used for temporal discretization. The time marching scheme over (t^n, t^{n+1}) is given by

$$
\begin{aligned}
S_i^{(1)} &= S_i^n + \Delta t L\left(S_i^n, \boldsymbol{u}^{n+1}\right), \\
S_i^{(2)} &= \frac{3}{4} S_i^n + \frac{1}{4} S_i^{(1)} + \frac{1}{4} \Delta t L\left(S_i^{(1)}, \boldsymbol{u}^{n+1}\right), \\
S_i^{n+1} &= \frac{1}{3} S_i^n + \frac{2}{3} S_i^{(2)} + \frac{2}{3} \Delta t L\left(S_i^{(2)}, \boldsymbol{u}^{n+1}\right),
\end{aligned}
\tag{26}
$$

where superscripts n and $n+1$ denote time step counters, and Δt is time step size.

5 Results and Discussions

5.1 Tracer Flow

Two fluids are miscible in the case of tracer flow and have equal viscosities, i.e., $\mu = \mu_i = \mu_r$. Dependence of relative permeability functions on saturation is linear: S_i and $(1 - S_i)$ for invading and resident phases. The resulting total mobility is $\lambda_T = 1/\mu$.

To determine the number of realizations needed for statistical convergence of numerical simulations, we compare simulation results, i.e., the growth of mixing length as a function of time, obtained from ensemble averaging with 2, 4, 8, and 16 realizations of the permeability field defined on a 512×512 grid. Physical parameters used in the simulation are presented in Table 1. Figure 1 shows saturation maps from two realizations of permeability field with $\beta = -0.5$, $\rho = 1.0$ at the same time of injection. Fluctuations arising from the permeability field grow and develop into fingers in both maps, and fingers of the two maps exhibit different geometries owing to spatial variance of the heterogeneity in different realizations. The growth of mixing length in each case is obtained by calculating the mixing length at a fixed time interval using equation (20). The resulting ensemble averaging of different realizations are presented in Figure 2. It is observed that the growths of the mixing length for ensembles with the number of realizations larger than eight exhibit insignificant differences. Therefore, statistical convergence is obtained by averaging simulation results over eight realizations of the permeability field.

Scaling analysis of mixing lengths is performed with two values of β, i.e., -0.25 and -0.5. For each β, four values of ρ, referred to as ρ_0, ρ_1, ρ_2, and ρ_3, are selected such that the corresponding scaling factor is given by 1/8, 1/4, 1/2, and 1, respectively. From the scaling relation given by equation (15), the strength (ρ_j) of a given scaling factor (σ_j) is expressed as

$$\rho_j = \sigma_j^{-\beta/2}. \tag{27}$$

Values of ρ_j are summarized in Table 2. Figures 3a and 4a present the mixing length in terms of injection time in log-log scale for $\beta = -0.25$ and -0.5, respectively. In each case larger values of ρ give longer mixing lengths due to stronger fluctuations of the permeability field. The mixing length curves are then scaled according to equation (21), and results are presented in Figures 3b and 4b. As shown, mixing length curves of different ρ tend to collapse to a single curve at intermediate times for both cases, indicating that numerical results follow the theoretical prediction. The discrepancies at early time (the transient regime) are attributed to the nonfractal behavior of the permeability field at short distances.

In log-log variables, the mixing length seems to be a linear function of time and its slope, denoted by dash line, is shown in Figures 3b and 4b. Results of the perturbation theory (Glimm & Sharp, 1991; Borges et al., 2009) suggest that the intermediate-time behavior of mixing length is given by a power law

$$l_\rho(t) \sim a(\rho)\, t^{\tau(\beta)}, \tag{28}$$

where $\tau(\beta)$ dependes on β in a nonlinear fashion; $\tau = \max\{\frac{1}{2}, \frac{1}{2} + \frac{1+\beta}{2}\}$. From equation (28) the growth rate (slope) on a log-log plot satisfies

$$\frac{\log l_\rho(t)}{\log t} \sim \gamma(\beta). \tag{29}$$

It is observed that the slope of the straight line ($\beta = -0.25$) is larger than that of the dashed line ($\beta = -0.5$), which agrees with the prediction from the perturbation theory. The slope in Figure 3b has not reached its expected value of 0.875 for the asymptotic regime. This indicates that the asymptotic regime has not been reached yet, but the scaling relation is valid regardless (Glimm & Sharp, 1991).

5.2 Multiphase Flow

Multiphase flow refers to the case in which the fluid pair, i.e., invading and resident fluids, may have different viscosities and their relative permeability functions have a nonlinear

Parameter	**Value**	**Unit**
Length, L	1.0	m
Porosity, ϕ	0.20	-
Absolute permeability, k_0	1.0e-14	m^2
Injection velocity, u_x^0	2.315e-5	m/s

Table 1: Physical parameters used in numerical simulation.

β	ρ_0	ρ_1	ρ_2	ρ_3
-0.25	0.771	0.841	0.917	1.0
-0.5	0.595	0.707	0.841	1.0

Table 2: Values of fluctuation strength.

dependence on saturation. As discussed in Hagoort (1974); Yortsos and Hickernell (1989); Riaz and Tchelepi (2004); Beliveau (2009); Berg and Ott (2012), the stability of displacement process is impacted by the properties of the fluid pair. The total shock mobility ratio, M_s^T, is used as the indicator of the onset of flow instability given as (Berg & Ott, 2012)

$$M_s^T = \frac{k_{ri}\left(S_{i,-}\right)/\mu_i + k_{rr}\left(S_{i,-}\right)/\mu_r}{k_{ri}\left(S_{i,+}\right)/\mu_i + k_{rr}\left(S_{i,+}\right)/\mu_r}, \tag{30}$$

where $S_{i,-}$ and $S_{i,+}$ represent invading phase saturation values behind and ahead of the saturation front from the analytical solution of the Buckley-Leverett equation (Buckley & Leverett, 1942), respectively. Values of M_s^T larger than unity indicate unstable displacement, i.e., small amplitude of perturbations in the saturation front grow into a fingered flow pattern, whereas values less than one indicate stable processes, i.e., such perturbations decay during displacements. Two pairs of immiscible fluids, namely stable and unstable flows, are considered in this work, see Table 3. Relative permeability functions are based on steady-state measurements of Berea sandstone cores (Tang & Kovscek, 2011).

Saturation maps from two realizations of permeability field are presented in Figure 5. Figures 5a and 5b show the results of stable flow. Fluctuations in velocity field develop into prominent channels with varying widths due to the heterogeneity of the permeability field. The interface between two phases exhibits sharper transitions compared to that in tracer

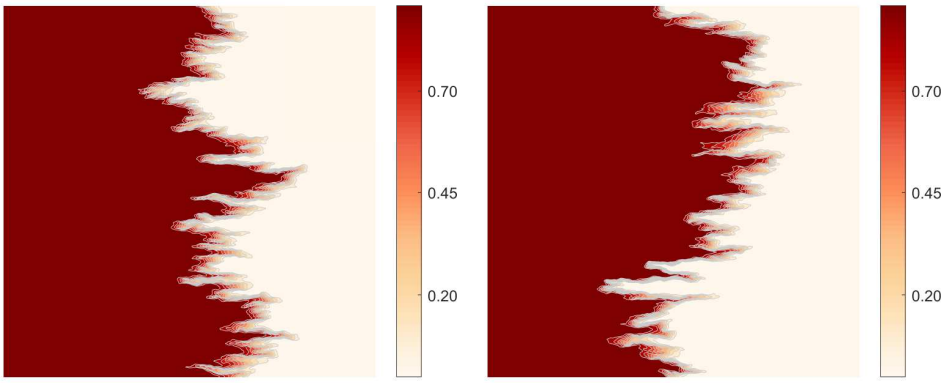

(a) (b)

Figure 1: Saturation maps of tracer flow from two realizations of permeability field ($\beta = -0.5$ and $\rho = 1.0$).

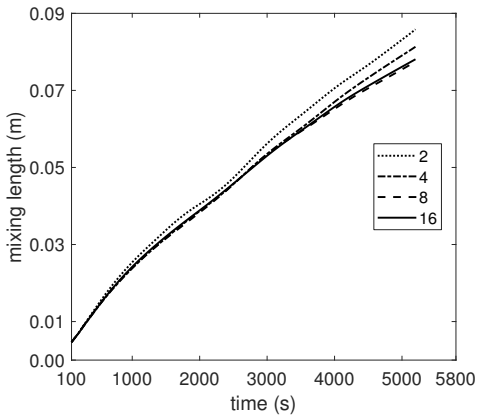

Figure 2: Ensembles of mixing length as a function of time with different numbers of realizations of the permeability field ($\beta = -0.5$ and $\rho = 1.0$).

flow shown in Figure 1. Results of unstable flow are presented in Figures 5c and 5d, where the random fields are identical as those used in stable flow. Fingers in unstable flow display a more complex structure compared to those in stable flow: large-scale fingers split at the tip and grow into individual fingers almost aligned with the mean flow direction, while some branches spread sidewise. The vigorous fingering behavior leads to substantial bypassing of the resident fluid, resulting in a relatively large mixing length. Figure 6 shows comparisons of ensemble averages of mixing length as a function of time obtained from different numbers

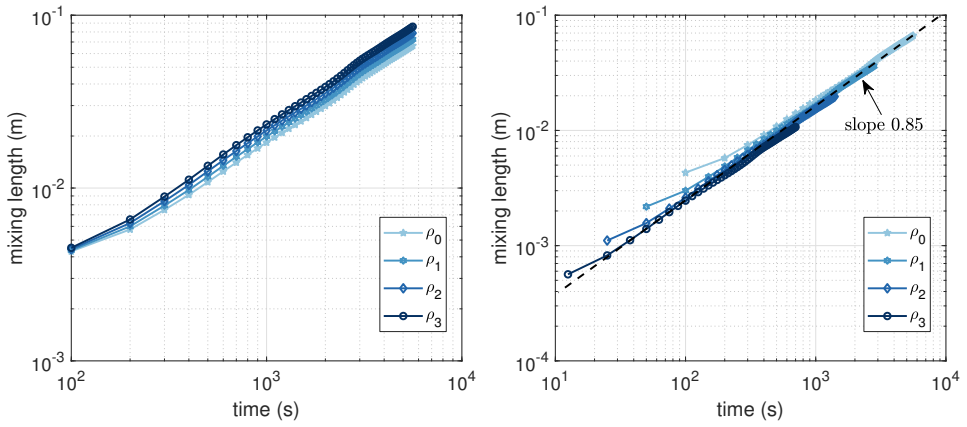

(a) (b)

Figure 3: Log-log plot of mixing length as a function of time for $\rho \approx 0.771$, 0.841, 0.917, and 1.0. (a) Mixing length curves, and (b) scaled curves according to (21) ($\beta = -0.25$).

of realizations. Results indicate that eight realizations appear to be sufficient in achieving statistical convergence for both types of flow.

One-dimensional mean saturation profiles, which are obtained by cross-sectional averaging of saturation maps, are plotted at times t, $2t$, $4t$, and $8t$ for $\rho \approx 0.595$, 0.707, 0.841, and 1.0, respectively - see Figures 7a and 7c. These profiles are scaled according to equation (19) shown in Figures 7b and 7d. In each case, the four distinct profiles collapse to a single curve, indicating that simulation results agree with the derived relation. Scaling analysis of mixing length is then performed in a fashion similar to that described in tracer flow: four values of ρ are investigated and their corresponding scaling factors, given by 1/8, 1/4, 1/2, and 1, are obtained from the analytically derived scaling law. Figures 8a and 9a display the mixing length in terms of injection time in log-log scale for stable and unstable flows, and the scaling results are presented in Figures 8b and 9b accordingly. As shown in Figures 8b and 9b, after an early transient regime, curves with different fluctuation strengths appear to collapse into a single curve. In the early transient regime, differences of mixing length obtained from different values of ρ are relatively pronounced. Growth rates of mixing length in the asymptotic regime are denoted by dash lines in Figures 8b and 9b. As shown, unstable flow has a higher growth rate than that of stable flow. This indicates

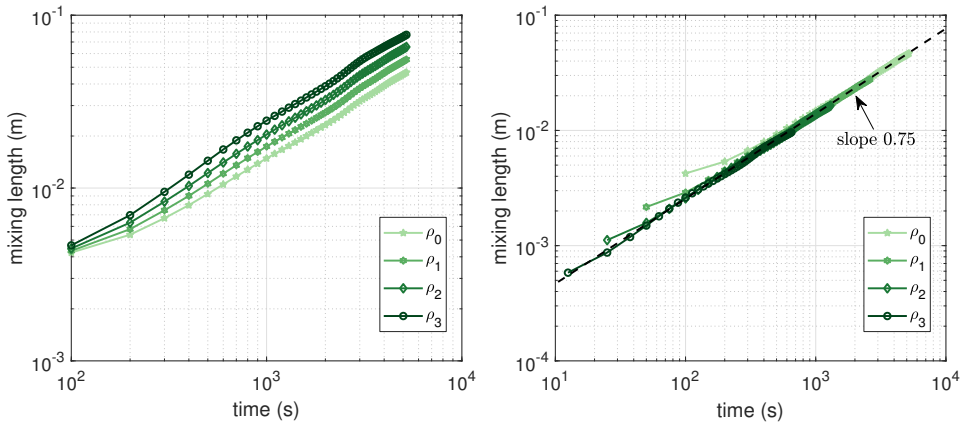

(a) (b)

Figure 4: Log-log plot of mixing length as a function of time for $\rho \approx 0.595$, 0.707, 0.841, and 1.0. (a) Mixing length curves, and (b) scaled curves according to (21) ($\beta = -0.5$).

that the nonlinearity dominates the flow in the asymptotic regime: the nonlinear effects are stabilizing/destabilizing the flow in stable/unstable cases, respectively.

Case #	Type	Viscosity Ratio	Total Shock Mobility Ratio
1	Stable	18.0	0.87
2	Unstable	120.0	2.10

Table 3: Physical parameters of fluid pairs.

6 Conclusion

In this work, we employ a recently developed high-resolution, two-dimensional numerical simulator to investigate the dynamics of two-phase flow in permeable media. Flow equation is cast in a vorticity stream-function form and solved using a spectral method. Transport equation is discretized using a third-order explicit scheme, and the convection flux is computed using a third-order central-upwind method. The coupled equations are solved in a sequential manner in each time step. To capture the fractal characteristics of natural permeable media, we utilize a random field with a power-law covariance function

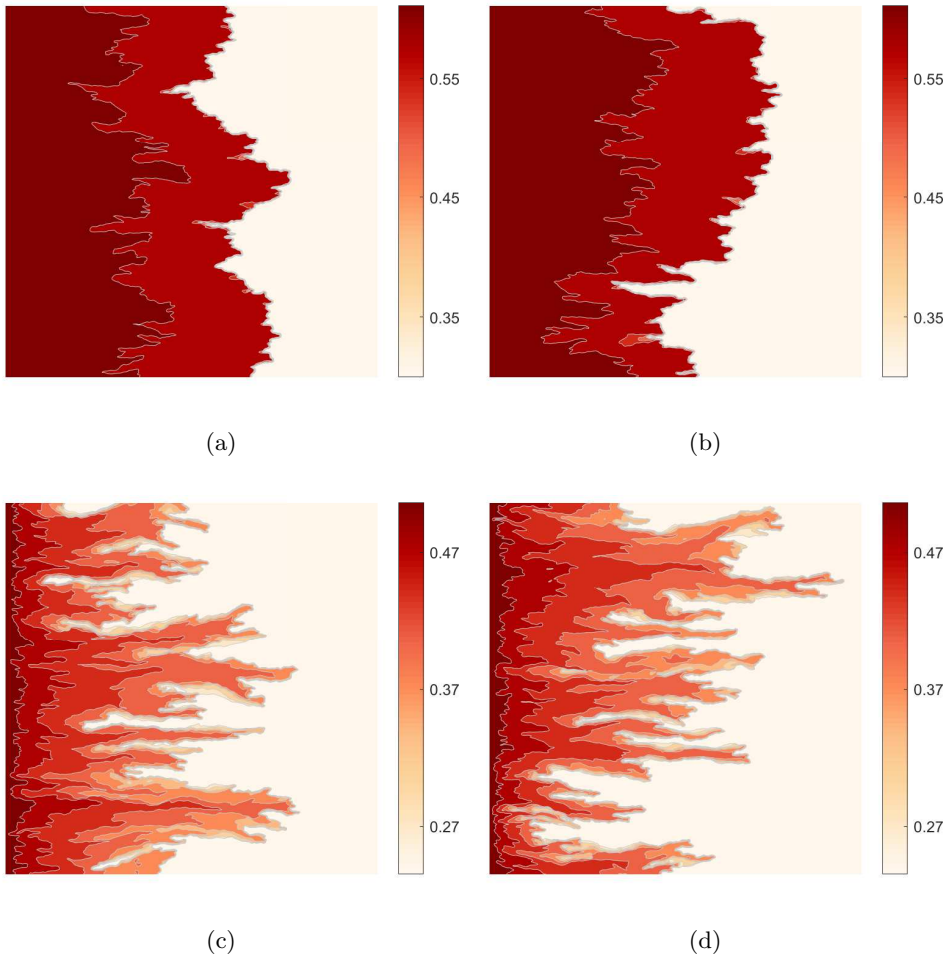

Figure 5: Saturation maps of multiphase flow from two realizations of permeability field. (a) and (b) stable flow, and (c) and (d) unstable flow ($\beta = -0.5$ and $\rho = 1.0$).

to describe the permeability field. A scaling relation, which relates permeability fields with different fluctuation strengths, is derived based on the statistical property (self-similarity) of the random field. The derived scaling relation in turn implies that flow problems governed by the flow and transport equations could be related: the dynamics of flow for different strengths of heterogeneity could be obtained from the result for a single fixed strength. In particular, scaling relations with respect to ensemble averages of mean saturation profiles and mixing lengths are proposed.

To verify the proposed scaling relations, we first conduct numerical experiments for tracer flow, where invading and resident fluids have equal viscosities, and relative permeability functions are linear functions of saturation. A sensitivity study is performed to

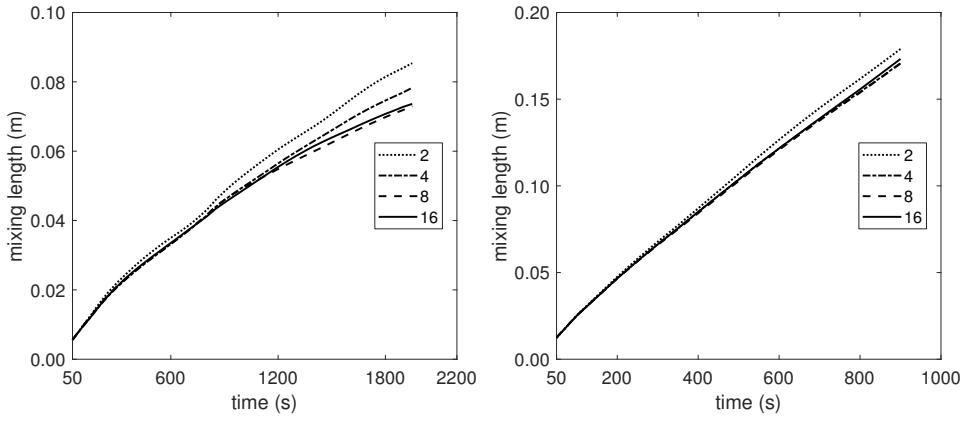

(a) (b)

Figure 6: Ensembles of mixing length as a function of time with different numbers of realizations of the permeability field. (a) Stable flow, and (b) unstable flow ($\beta = -0.5$ and $\rho = 1.0$).

determine the required number of realizations for statistical convergence. Results show that the growth of mixing length obtained from averaging of eight realizations result in a satisfactory convergence. The derived scaling relations are then examined using ensemble averages of simulation results from those realizations. Results suggest that the mixing length curves from different fluctuation strengths and two different values of $|\beta|$ scale in accordance with the desired relation. The mixing length curve obtained from the case with a smaller values of $|\beta|$ has a larger slope in the asymptotic regime, which is consistent with result from perturbation theory.

Next we investigate nonlinear transport, where the dispersion of fluid mixing is a consequence of collective efforts from nonlinearity and heterogeneity. Relative permeability functions are extracted from literature, which is based on experimental measurements. We consider two cases with M_s^T smaller/greater than unity indicating stable/unstable flow. Saturation maps of the stable flow show that heterogeneity in the permeability field facilitates the development of highly conductive flow channels, thus introducing dispersion in fluid mixing. On the other hand, simulation results of unstable flow exhibit highly-fingered flow pattern, which leads to a lager mixing length compared to that of stable flow with the same permeability field. The mixing length curves for both cases are scaled according to

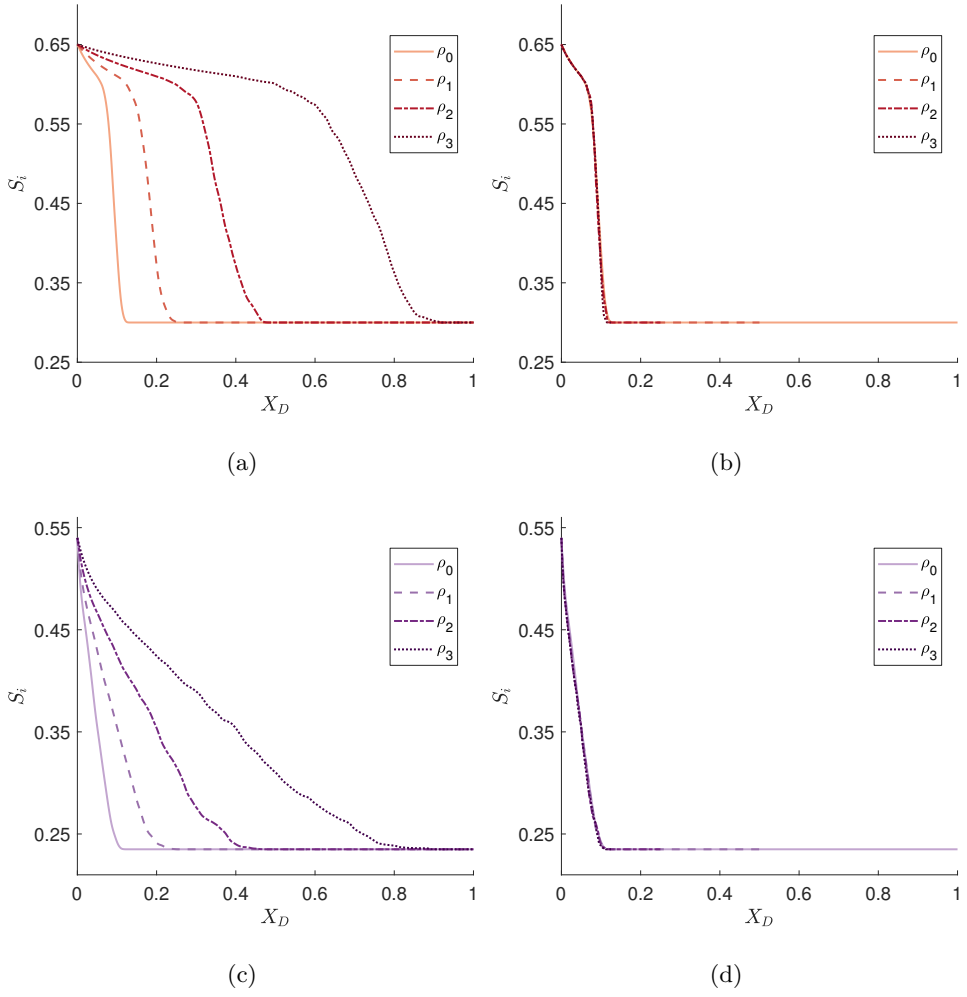

Figure 7: Mean saturation profiles and scaled curves according to equation (19) for $\rho \approx 0.595, 0.707, 0.841$, and 1.0. (a) and (b) stable flow, and (c) and (d) unstable flow ($\beta = -0.5$).

the derived relation, and results show that these curves appear to collapse to a single curve at intermediate times.

To summarize, numerical simulation results from both linear (tracer flow) and nonlinear transport flow agree with predictions from analytically derived scaling relations in the asymptotic regime. The correlation structure of heterogeneity plays a significant role in determining the scaling behavior in linear flow, whereas in the case of nonlinear flow, scaling behavior appears to be dominated by the degree of nonlinearity.

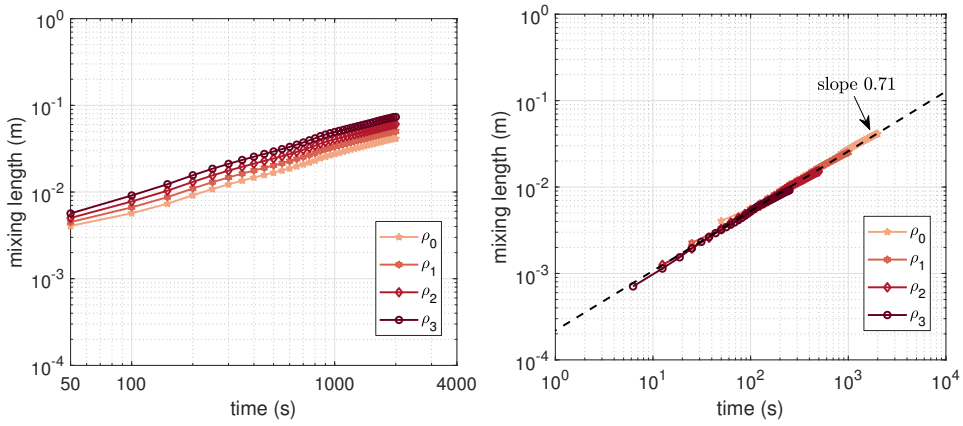

(a) (b)

Figure 8: Log-log plot of mixing length as a function of time in the case of stable flow for $\rho \approx 0.595$, 0.707, 0.841, and 1.0. (a) Mixing length curves, and (b) scaled curves according to equation (21) ($\beta = -0.5$).

Appendix A Discretization of the Convection Flux

The central-upwind scheme (Kurganov & Tadmor, 2000; Kurganov et al., 2001) is used to discretize the convection flux. For brevity, we consider one-dimensional system with uniform spacing cells. The semi-discrete form of central-upwind scheme is given by

$$\frac{\mathrm{d}}{\mathrm{d}t} S_i|_j = -\frac{u_x|_j}{\phi \Delta x} \left(F(\xi_\theta)|_{j+\frac{1}{2}} - F(\xi_\theta)|_{j-\frac{1}{2}} \right), \tag{A1}$$

where

$$F(\xi_\theta)|_{j+\frac{1}{2}} = \frac{a^+_{j+\frac{1}{2}} f\left(\xi^-_{j+\frac{1}{2}}\right) - a^-_{j+\frac{1}{2}} f\left(\xi^+_{j+\frac{1}{2}}\right)}{a^+_{j+\frac{1}{2}} - a^-_{j+\frac{1}{2}}} + \frac{a^+_{j+\frac{1}{2}} a^-_{j+\frac{1}{2}}}{a^+_{j+\frac{1}{2}} - a^-_{j+\frac{1}{2}}} \left[\xi^+_{j+\frac{1}{2}} - \xi^-_{j+\frac{1}{2}} \right], \tag{A2}$$

and $f(\xi) = f_i(\xi)$. In equation (A2), $\xi^-_{j+\frac{1}{2}}$ and $\xi^+_{j+\frac{1}{2}}$ denote left and right intermediate values at cell interface $x_{j+\frac{1}{2}}$. $a^-_{j+\frac{1}{2}}$ and $a^+_{j+\frac{1}{2}}$ are local speeds of propagation at cell interface $x_{j+\frac{1}{2}}$. In this work we take (Kurganov et al., 2001, 2007)

$$a^+_{j+\frac{1}{2}} = -a^-_{j+\frac{1}{2}} = a_{j+\frac{1}{2}}, \tag{A3}$$

where

$$a_{j+\frac{1}{2}} = \max_{\xi \in \left[\xi^-_{j+\frac{1}{2}}, \xi^+_{j+\frac{1}{2}}\right]} f'(\xi). \tag{A4}$$

Substituting Eq. (A3) into Eq. (A2), the numerical flux becomes

$$F(\xi_\theta)|_{j+\frac{1}{2}} = \frac{f\left(\xi^+_{j+\frac{1}{2}}\right) + f\left(\xi^-_{j+\frac{1}{2}}\right)}{2} - \frac{a_{j+\frac{1}{2}}}{2} \left[\xi^+_{j+\frac{1}{2}} - \xi^-_{j+\frac{1}{2}} \right]. \tag{A5}$$

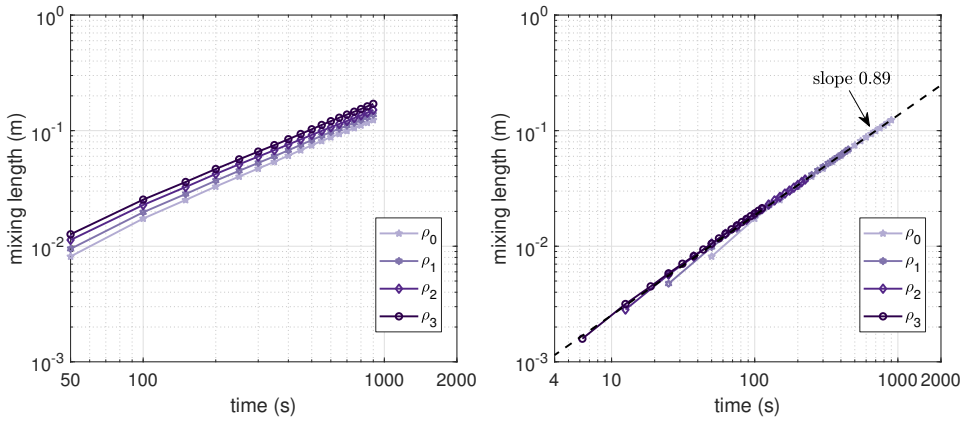

(a) (b)

Figure 9: Log-log plot of mixing length as a function of time in the case of unstable flow for $\rho \approx 0.595$, 0.707, 0.841, and 1.0. (a) Mixing length curves, and (b) scaled curves according to equation (21) ($\beta = -0.5$).

$F(\xi_\theta)|_{j-\frac{1}{2}}$ is obtained in a similar fashion expressed as

$$F(\xi_\theta)|_{j-\frac{1}{2}} = \frac{f\left(\xi^+_{j-\frac{1}{2}}\right) + f\left(\xi^-_{j-\frac{1}{2}}\right)}{2} - \frac{a_{j-\frac{1}{2}}}{2}\left[\xi^+_{j-\frac{1}{2}} - \xi^-_{j-\frac{1}{2}}\right]. \tag{A6}$$

Intermediate values, $\xi^+_{j+\frac{1}{2}}$ and $\xi^-_{j+\frac{1}{2}}$, are constructed using the third-order central weighted essentially nonoscillatory (CWENO) scheme (Kurganov & Levy, 2000) given by

$$\xi^+_{j+\frac{1}{2}} = A_{j+1} - \frac{\Delta x}{2}B_{j+1} + \frac{(\Delta x)^2}{8}C_{j+1}, \tag{A7}$$

and

$$\xi^-_{j+\frac{1}{2}} = A_j + \frac{\Delta x}{2}B_j + \frac{(\Delta x)^2}{8}C_j, \tag{A8}$$

where A_j, B_j, and C_j are given by

$$\begin{cases} A_j = \xi_j - \frac{w_C}{12}\left(\xi_{j+1} - 2\xi_j + \xi_{j-1}\right), \\ B_j = \frac{1}{\Delta x}\left[w_R\left(\xi_{j+1} - \xi_j\right) + w_C\frac{\xi_{j+1}-\xi_{j-1}}{2} + w_L\left(\xi_j - \xi_{j-1}\right)\right], \\ C_j = 2w_C\frac{\xi_{j-1}-2\xi_j+\xi_{j+1}}{\Delta x^2}. \end{cases} \tag{A9}$$

In equations (A9), subscript L, R, and C denote the left side, the right side, and the center location of cell j. w_k ($k \in \{L, C, R\}$) are the weights espressed as

$$w_k = \frac{\chi_k}{\sum_m \chi_m},\ \chi_k = \frac{c_k}{(\varepsilon + IS_k)^p}, \tag{A10}$$

where $c_L = c_R = 1/4$, $c_C = 1/2$, and $p = 2$. ε is used to ensure that the denominator of χ_k is nonzero: $\varepsilon = 10^{-6}$. The smooth indicators IS_k are given by

$$\begin{cases} IS_L = (\xi_j - \xi_{j-1})^2, \\ IS_R = (\xi_{j+1} - \xi_j)^2, \\ IS_C = \frac{13}{3}(\xi_{j+1} - 2\xi_j + \xi_{j-1})^2 + \frac{1}{4}(\xi_{j+1} - \xi_{j-1})^2. \end{cases} \tag{A11}$$

Acknowledgments

This work was supported as part of the Center for Mechanistic Control of Water-Hydrocarbon-Rock Interactions in Unconventional and Tight Oil Formations (CMC-UF), an Energy Frontier Research Center funded by the U.S. Department of Energy, Office of Science under DOE (BES) Award DE-SC0019165. Data archiving is underway in the research data repository Mountain Scholar, where the data will be available with a unique and permanent document identifier.

References

Amooie, M. A., Soltanian, M. R., & Moortgat, J. (2017). Hydrothermodynamic mixing of fluids across phases in porous media. *Geophysical Research Letters*, *44*(8), 3624–3634.

Babadagli, T. (2006). Effective permeability estimation for 2-D fractal permeability fields. *Mathematical geology*, *38*(1), 33–50.

Beliveau, D. (2009). Waterflooding viscous oil reservoirs. *SPE Reservoir Evaluation & Engineering*, *12*(05), 689–701.

Berg, S., & Ott, H. (2012). Stability of CO2–brine immiscible displacement. *International Journal of Greenhouse Gas Control*, *11*, 188–203.

Bijeljic, B., & Blunt, M. J. (2006). Pore-scale modeling and continuous time random walk analysis of dispersion in porous media. *Water resources research*, *42*(1).

Borges, M., Furtado, F., Pereira, F., & Souto, H. A. (2009). Scaling analysis for the tracer flow problem in self-similar permeability fields. *Multiscale Modeling & Simulation*, *7*(3), 1130–1147.

Buckley, S. E., & Leverett, M. (1942). Mechanism of fluid displacement in sands. *Transactions of the AIME*, *146*(01), 107–116.

Celia, M. A., Reeves, P. C., & Ferrand, L. A. (1995). Recent advances in pore scale models for multiphase flow in porous media. *Reviews of Geophysics*, *33*(S2), 1049–1057.

Chen, Y., & Durlofsky, L. J. (2006). Adaptive local–global upscaling for general flow scenarios in heterogeneous formations. *Transport in porous Media*, *62*(2), 157–185.

Christou, K., Radünz, W., Lashore, B., de Oliveira, F., & Gomes, J. (2019). Numerical investigation of viscous flow instabilities in multiphase heterogeneous porous media. *Advances in Water Resources*, *130*, 46–65.

Connolly, M., & Johns, R. T. (2016). Scale-dependent mixing for adverse mobility ratio flows in heterogeneous porous media. *Transport in Porous Media*, *113*(1), 29–50.

Cushman, J. H. (2013). *The physics of fluids in hierarchical porous media: Angstroms to miles* (Vol. 10). Springer Science & Business Media.

Daripa, P., & Dutta, S. (2017). Modeling and simulation of surfactant–polymer flooding using a new hybrid method. *Journal of Computational Physics*, *335*, 249–282.

Dentz, M., Le Borgne, T., Englert, A., & Bijeljic, B. (2011). Mixing, spreading and reaction in heterogeneous media: A brief review. *Journal of contaminant hydrology*, *120*, 1–17.

Dullien, F. A. (2012). *Porous media: fluid transport and pore structure*. Academic press.

Eggleston, J., & Rojstaczer, S. (1998). Inferring spatial correlation of hydraulic conductivity from sediment cores and outcrops. *Geophysical research letters*, *25*(13), 2321–2324.

Francisco, A., Ginting, V., Pereira, F., & Rigelo, J. (2014). Design and implementation of a multiscale mixed method based on a nonoverlapping domain decomposition procedure. *Mathematics and Computers in Simulation*, *99*, 125–138.

Furtado, F., & Pereira, F. (1998). Scaling analysis for two-phase immiscible flow in heterogeneous porous media. *Computational and Applied Mathematics*, *17*, 237–264.

Furtado, F., & Pereira, F. (2003). Crossover from nonlinearity controlled to heterogeneity controlled mixing in two-phase porous media flows. *Computational Geosciences*, *7*(2), 115–135.

Glimm, J., & Sharp, D. H. (1991). A random field model for anomalous diffusion in heterogeneous porous media. *Journal of statistical Physics*, *62*(1-2), 415–424.

Gottlieb, D., & Orszag, S. A. (1977). *Numerical analysis of spectral methods: theory and applications* (Vol. 26). Siam.

Gottlieb, S., & Shu, C.-W. (1998). Total variation diminishing Runge-Kutta schemes. *Mathematics of computation*, *67*(221), 73–85.

Gottlieb, S., Shu, C.-W., & Tadmor, E. (2001). Strong stability-preserving high-order time discretization methods. *SIAM review*, *43*(1), 89–112.

Guo, B., Bandilla, K. W., Doster, F., Keilegavlen, E., & Celia, M. A. (2014). A vertically

integrated model with vertical dynamics for CO2 storage. *Water Resources Research*, *50*(8), 6269–6284.

Guo, F., & Aryana, S. A. (2019). An experimental investigation of flow regimes in imbibition and drainage using a microfluidic platform. *Energies*, *12*(7), 1390.

Hagoort, J. (1974). Displacement stability of water drives in water-wet connate-water-bearing reservoirs. *Society of Petroleum Engineers Journal*, *14*(01), 63–74.

Hajibeygi, H., Lee, S. H., & Lunati, I. (2012). Accurate and efficient simulation of multiphase flow in a heterogeneous reservoir with error estimate and control in the multiscale finite-volume framework. *Spe Journal*, *17*(04), 1–071.

Harte, D. (2001). *Multifractals: theory and applications*. CRC Press.

Harten, A. (1983). High resolution schemes for hyperbolic conservation laws. *Journal of computational physics*, *49*(3), 357–393.

Hassan, A. E., Cushman, J. H., & Delleur, J. W. (1997). Monte Carlo studies of flow and transport in fractal conductivity fields: Comparison with stochastic perturbation theory. *Water Resources Research*, *33*(11), 2519–2534.

Heidari, P., & Li, L. (2014). Solute transport in low-heterogeneity sandboxes: The role of correlation length and permeability variance. *Water Resources Research*, *50*(10), 8240–8264.

Helmig, R. (1997). *Multiphase flow and transport processes in the subsurface: a contribution to the modeling of hydrosystems*. Springer-Verlag.

Hewett, T. A., & Behrens, R. A. (1990). Conditional simulation of reservoir heterogeneity with fractals. *SPE formation evaluation*, *5*(03), 217–225.

Hubbert, M. K. (1957). Darcy's law and the field equations of the flow of underground fluids. *Hydrological Sciences Journal*, *2*(1), 23–59.

Jha, B., Cueto-Felgueroso, L., & Juanes, R. (2011). Fluid mixing from viscous fingering. *Physical review letters*, *106*(19), 194502.

Juanes, R. (2008). Nonequilibrium effects in models of three-phase flow in porous media. *Advances in Water Resources*, *31*(4), 661–673.

Kurganov, A., & Levy, D. (2000). A third-order semidiscrete central scheme for conservation laws and convection-diffusion equations. *SIAM Journal on Scientific Computing*, *22*(4), 1461–1488.

Kurganov, A., Noelle, S., & Petrova, G. (2001). Semidiscrete central-upwind schemes for hyperbolic conservation laws and Hamilton–Jacobi equations. *SIAM Journal on*

Scientific Computing, *23*(3), 707–740.

Kurganov, A., & Petrova, G. (2001). A third-order semi-discrete genuinely multidimensional central scheme for hyperbolic conservation laws and related problems. *Numerische Mathematik*, *88*(4), 683–729.

Kurganov, A., Petrova, G., & Popov, B. (2007). Adaptive semidiscrete central-upwind schemes for nonconvex hyperbolic conservation laws. *SIAM Journal on Scientific Computing*, *29*(6), 2381–2401.

Kurganov, A., & Tadmor, E. (2000). New high-resolution central schemes for nonlinear conservation laws and convection–diffusion equations. *Journal of Computational Physics*, *160*(1), 241–282.

Kutz, J. N. (2013). *Data-driven modeling & scientific computation: methods for complex systems & big data*. Oxford University Press.

Lenormand, R. (1990). Liquids in porous media. *Journal of Physics: Condensed Matter*, *2*(S), SA79.

LeVeque, R. J. (1992). *Numerical methods for conservation laws* (Vol. 3). Springer.

Leverett, M. (1941). Capillary behavior in porous solids. *Transactions of the AIME*, *142*(01), 152–169.

Liang, Y., Wen, B., Hesse, M. A., & DiCarlo, D. (2018). Effect of dispersion on solutal convection in porous media. *Geophysical Research Letters*, *45*(18), 9690–9698.

Liu, H., Valocchi, A. J., Werth, C., Kang, Q., & Oostrom, M. (2014). Pore-scale simulation of liquid co2 displacement of water using a two-phase lattice Boltzmann model. *Advances in Water Resources*, *73*, 144–158.

Mandelbrot, B. B. (1985). Self-affine fractals and fractal dimension. *Physica scripta*, *32*(4), 257.

Mehmani, Y., & Tchelepi, H. A. (2019). Multiscale formulation of two-phase flow at the pore scale. *Journal of Computational Physics*, *389*, 164–188.

Meiburg, E., & Homsy, G. (1988). Nonlinear unstable viscous fingers in Hele–Shaw flows. II. Numerical simulation. *The Physics of fluids*, *31*(3), 429–439.

Mercer, J. W., & Cohen, R. M. (1990). A review of immiscible fluids in the subsurface: properties, models, characterization and remediation. *Journal of contaminant hydrology*, *6*(2), 107–163.

Muskat, M., & Meres, M. W. (1936). The flow of heterogeneous fluids through porous media. *Physics*, *7*(9), 346–363.

Neuman, S. P. (1995). On advective transport in fractal permeability and velocity fields. *Water Resources Research*, *31*(6), 1455–1460.

Nicolaides, C., Jha, B., Cueto-Felgueroso, L., & Juanes, R. (2015). Impact of viscous fingering and permeability heterogeneity on fluid mixing in porous media. *Water Resources Research*, *51*(4), 2634–2647.

Nijjer, J. S., Hewitt, D. R., & Neufeld, J. A. (2019). Stable and unstable miscible displacements in layered porous media. *Journal of Fluid Mechanics*, *869*, 468–499.

Prodanović, M., & Bryant, S. L. (2006). A level set method for determining critical curvatures for drainage and imbibition. *Journal of colloid and interface science*, *304*(2), 442–458.

Riaz, A., & Tchelepi, H. A. (2004). Linear stability analysis of immiscible two-phase flow in porous media with capillary dispersion and density variation. *Physics of Fluids*, *16*(12), 4727–4737.

Riaz, A., & Tchelepi, H. A. (2006). Numerical simulation of immiscible two-phase flow in porous media. *Physics of Fluids*, *18*(1), 014104.

Rogerson, A., & Meiburg, E. (1993). Numerical simulation of miscible displacement processes in porous media flows under gravity. *Physics of Fluids A: Fluid Dynamics*, *5*(11), 2644–2660.

Sajjadi, M., & Azaiez, J. (2013). Scaling and unified characterization of flow instabilities in layered heterogeneous porous media. *Physical Review E*, *88*(3), 033017.

Shu, C.-W. (2009). High order weighted essentially nonoscillatory schemes for convection dominated problems. *SIAM review*, *51*(1), 82–126.

Sweby, P. K. (1984). High resolution schemes using flux limiters for hyperbolic conservation laws. *SIAM journal on numerical analysis*, *21*(5), 995–1011.

Tan, C., & Homsy, G. (1988). Simulation of nonlinear viscous fingering in miscible displacement. *The Physics of fluids*, *31*(6), 1330–1338.

Tang, G.-Q., & Kovscek, A. (2011). High resolution imaging of unstable, forced imbibition in Berea sandstone. *Transport in porous media*, *86*(2), 617–634.

Tryggvason, G., & Aref, H. (1983). Numerical experiments on Hele Shaw flow with a sharp interface. *Journal of Fluid Mechanics*, *136*, 1–30.

Voss, R. F. (1988). Fractals in nature: from characterization to simulation. In *The science of fractal images* (pp. 21–70). Springer.

Wang, Y., Aryana, S. A., & Allen, M. B. (2019). An extension of Darcy's law incorporating

dynamic length scales. *Advances in Water Resources*, *129*, 70–79.

Wang, Y., Aryana, S. A., Furtado, F., & Ginting, V. (2018). Analysis of nonequilibrium effects and flow instability in immiscible two-phase flow in porous media. *Advances in Water Resources*, *122*, 291–303.

Wen, B., Akhbari, D., Zhang, L., & Hesse, M. A. (2018). Convective carbon dioxide dissolution in a closed porous medium at low pressure. *Journal of Fluid Mechanics*, *854*, 56–87.

Whitaker, S. (1986). Flow in porous media I: A theoretical derivation of Darcy's law. *Transport in porous media*, *1*(1), 3–25.

Wilkinson, D., & Willemsen, J. F. (1983). Invasion percolation: a new form of percolation theory. *Journal of Physics A: Mathematical and General*, *16*(14), 3365.

Wyckoff, R., & Botset, H. (1936). The flow of gas-liquid mixtures through unconsolidated sands. *Physics*, *7*(9), 325–345.

Xue, L., Li, D., Nan, T., & Wu, J. (2019). Predictive assessment of groundwater flow uncertainty in multiscale porous media by using truncated power variogram model. *Transport in Porous Media*, *126*(1), 97–114.

Yortsos, Y., & Hickernell, F. (1989). Linear stability of immiscible displacement in porous media. *SIAM Journal on Applied Mathematics*, *49*(3), 730–748.

Yuan, Q., & Azaiez, J. (2014). Miscible displacements in porous media with time-dependent injection velocities. *Transport in porous media*, *104*(1), 57–76.

Yuan, Q., Zhou, X., Wang, J., Zeng, F., Knorr, K. D., & Imran, M. (2019). Control of viscous fingering and mixing in miscible displacements with time-dependent rates. *AIChE Journal*, *65*(1), 360–371.

Zhang, C., Oostrom, M., Wietsma, T. W., Grate, J. W., & Warner, M. G. (2011). Influence of viscous and capillary forces on immiscible fluid displacement: Pore-scale experimental study in a water-wet micromodel demonstrating viscous and capillary fingering. *Energy & Fuels*, *25*(8), 3493–3505.

Zhang, D., & Tchelepi, H. (1999). Stochastic analysis of immiscible two-phase flow in heterogeneous media. *SPE Journal*, *4*(04), 380–388.

Zhang, Q. (1992). A multi-length-scale theory of the anomalous mixing-length growth for tracer flow in heterogeneous porous media. *Journal of Statistical Physics*, *66*(1-2), 485–501.